nature geoscience

ARTICLES

https://doi.org/10.1038/s41561-021-00892-0



# Pyrogenic carbon decomposition critical to resolving fire's role in the Earth system

Simon P. K. Bowring[1,2,3]✉, Matthew W. Jones[4], Philippe Ciais[3], Bertrand Guenet[2] and Samuel Abiven[2,5]

**Recently identified post-fire carbon fluxes indicate that, to understand whether global fires represent a net carbon source or sink, one must consider both terrestrial carbon retention through pyrogenic carbon production and carbon losses via multiple pathways. Here these legacy source and sink pathways are quantified using a CMIP6 land surface model to estimate Earth's fire carbon budget. Over the period 1901–2010, global pyrogenic carbon has driven an annual soil carbon accumulation of 337 TgC yr$^{-1}$, offset by legacy carbon losses totalling −248 TgC yr$^{-1}$. The residual of these values constrains the maximum annual pyrogenic carbon mineralization to 89 TgC yr$^{-1}$ and the pyrogenic carbon mean residence time to 5,387 years, assuming a steady state. The residual is negative over forests and positive over grassland-savannahs (implying a potential sink), suggesting contrasting roles of vegetation in the fire carbon cycle. The paucity of observational constraints for representing pyrogenic carbon mineralization means that, without assuming a steady state, we are unable to determine the sign of the overall fire carbon balance. Constraining pyrogenic carbon mineralization rates, particularly over grassland-savannahs, is a critical research frontier that would enable a fuller understanding of fire's role in the Earth system and inform attendant land use and conservation policy.**

Wildfires are a key driver of disturbance–recovery cycles in many regions of the world. Although fires emit large quantities of $CO_2$ carbon ($CO_2$-C) to the atmosphere (~2 PgC yr$^{-1}$, hereafter $E^{-}_{\mathrm{Fire}}$)[1], subsequent vegetation recovery recaptures the emitted carbon on decadal timescales[2–4] and results in an uncertain but probably small net impact on atmospheric carbon in the long run[5], which is insignificant compared to other biogeochemical feedbacks in geological time[6–8]. Natural shifts in fire regimes and vegetation occur infrequently[9], and current changes are largely driven by climatic[10] and human[11] perturbations. However, even in the absence of global fire regime changes, a range of long-term 'legacy' post-fire carbon fluxes lead to either carbon accumulation or loss by land ecosystems locally, with their balance as yet undetermined[12].

On the terrestrial legacy carbon sink side, the charring of biomass by fire creates a by-product known as pyrogenic carbon (PyC) (~10–20% annual fire $CO_2$ emissions)[12,13], which is significantly more resistant to biochemical oxidation than bulk soil organic carbon (SOC)[14–17]. Most studies find that PyC degrades with a highly uncertain mean residence time (MRT), ranging from decades to thousands of years[18–23] (one to three orders of magnitude higher than non-PyC SOC), suggesting that its production drives a sequestration flux from the atmosphere that exceeds the temporal boundaries of the fire-recovery cycle in most fire regimes, resulting in long-term terrestrial PyC accumulation ($\mathrm{SOC}^{+}_{\mathrm{PyC}}$). In addition to the production of refractory PyC accumulating in soils ($\mathrm{SOC}^{+}_{\mathrm{PyC}}$), there is also a lightweight 'labile' component that is likewise readily mobilized, hereafter denoted ($\mathrm{PyC}^{+}_{\mathrm{LW}}$; Supplementary Section 2).

On the terrestrial 'legacy carbon loss' side, like other forms of SOC, PyC is liable to mineralization to the atmosphere ($E^{-}_{\mathrm{PyC}}$) and to export from land to oceans via rivers ($\mathrm{SOC}^{-}_{\mathrm{PyCExp}}$) in particulate or dissolved form (Py-POC and Py-DOC, respectively), totalling >40 TgPyC-C yr$^{-1}$ (refs. [18,24]). A fraction of this river-transported PyC is eventually deposited to the ocean floor over up to 10,000 years[18,21] after its initial production, with some presently unknown proportion of photo-oxidation occurring en route in fresh and marine surface waters and in sediments[25]. The steady-state condition of the terrestrial fire carbon cycle thus has the following formulation:

$$E^{-}_{\mathrm{Fire}} + E^{-}_{\mathrm{PyC}} + \mathrm{SOC}^{-}_{\mathrm{PyCExp}} = U^{+}_{\mathrm{VCO_2}} + \mathrm{SOC}^{+}_{\mathrm{PyC}} + \mathrm{PyC}^{+}_{\mathrm{LW}} \quad (1)$$

where $E^{-}_{\mathrm{Fire}}$ is the fire carbon emissions due to vegetation combustion, $E^{-}_{\mathrm{PyC}}$ represents refractory and lightweight PyC mineralization in the terrestrial domain[25] and $U_{\mathrm{VCO_2}}$ is the uptake of atmospheric $CO_2$ by post-fire vegetation recovery, with poles referring to flux direction (gain (+)/loss (−)) with respect to carbon stocks in the terrestrial biosphere.

The production rate of PyC is intimately linked with vegetation type, mean climate and climate variability[6,26]. Bio-climatic zones determine the rate of biomass (fuel) build-up as well as the probable time between fire events, referred to here as the fire return interval (FRI), with a positive relation between fuel accumulation and FRI across a gradient of increasing FRI from, for example, grassland-savannah to dry forest and rainforest biomes (Fig. 1a). FRI in turn proxies biome-scale PyC production rates (Fig. 1d), and increasing dry fuel accumulation per unit area enables greater combustion, heat release and flame temperatures, all else (fuel and climate conditions) being equal (model $H_1$; Fig. 1c).

Less is known about how the mean residence time of PyC is affected by FRI. One plausible conceptual model is that MRT is a positive function of flame temperature[14,20], such that low-FRI

[1]Soil Science and Biogeochemistry Group, Department of Geography, University of Zurich, Zurich, Switzerland. [2]Laboratoire de Géologie, Département de Géosciences, Ecole Normale Supérieure (ENS), Paris, France. [3]Laboratoire des Sciences du Climat et de l'Environnement (LSCE), IPSL, Gif sur Yvette, France. [4]Tyndall Centre for Climate Change Research, School of Environmental Sciences, University of East Anglia, Norwich, UK. [5]CEREEP-Ecotron Ile De France, St-Pierre-lès-Nemours, France. ✉e-mail: simon_bowring@hotmail.com

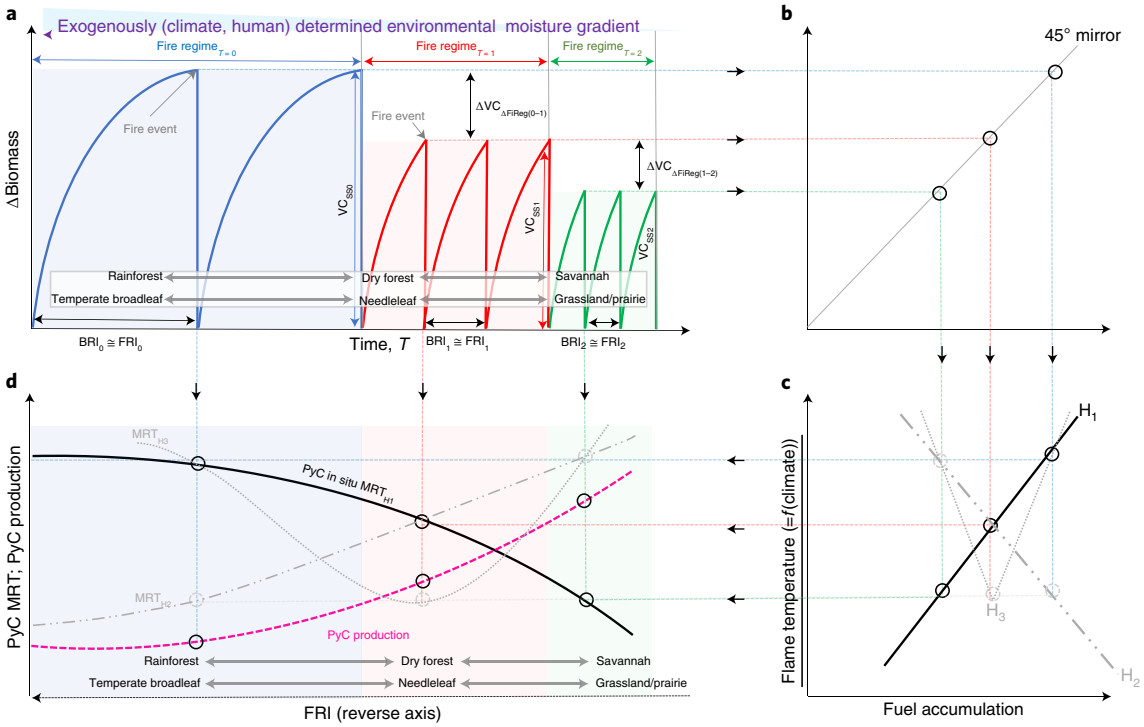


**Fig. 1 | Conceptual representation of the interrelation between plot or biome-scale vegetation, fire and PyC dynamics. a**, Change of vegetation biomass carbon (a mass quantity) post-fire to the steady state ($VC_{SSn}$) and its evolution with change in fire regime (Fire Regime.$_T$), where subscript ($T$) refers to the specific fire regime as $f$(time ($x$ axis)). Coloured shading indicates a hypothetical transition between stable vegetative states in a given biome or latitudinal bin along an environmental humidity and fire regime gradient. Included is the vegetative carbon-loss term due to a change between fire regimes $T$ and $T+1$ ($\Delta VC_{\Delta FiReg(T-T+1)}$), where FiReg is an abbreviation of Fire Regime.$_T$. The transition between vegetative states illustrates a shift from an idealized high BRI,FRI biome to a lower one. **b**, Graphic aid to mirror the $y$ axis in **a** onto the $x$ axis in **c**. **c**, Fire temperature (degrees) and terrestrial fuel accumulation (assumed here to be directly proportionate to ΔBiomass in **a**). The three curves denote different idealized possible relationships between the two variables, varying as a result of fuel conditions. Curve $H_1$ (black) describes a situation in which the conditions of fuel and fire (for example, fuel moisture and wind velocity) are equal across biomes. $H_2$ (dot-dashed grey line) assumes that the fuel condition differs with biome and assumes that grassland fuels are the driest and rainforest fuels the wettest, such that fuel accumulation is inversely related to flame temperature. $H_3$ (dotted grey line) describes a situation in which flame temperatures are highest in tropical forests and grassland, under the situation that severe drought conditions (and hence dry fuel) are a prerequisite for tropical wildfires, while grassland fuels tend to be very dry, whereas temperate biomes support fires even if they are relatively wet and of a lower temperature. **d**, Idealized PyC production (a mass rate, dashed pink) and its mean residence time ($MRT_{H1(black)-3(grey)}$) for different potential relationships between FRI, fuel accumulation and flame temperature in **c**. PyC production is assumed to increase with decreasing environmental moisture and FRI. Black circles relate a specific level of PyC production for a given vegetative state to its corresponding MRT and flame temperature. The graphs in **a**, **c** and **d** are thus related to one another by the coloured dashed lines. Curves $MRT_{H1}$, $MRT_{H2}$ and $MRT_{H3}$ relate to the respective flame temperature/fuel accumulation curves in **c**. See refs. [13–15,27,33,38,86,87].

biomes will tend to generate PyC of lower MRT (for example, black, pink curves in the grassland portion of Fig. 1d), all else being equal. However, flame temperatures are also determined by climate over the mid-length (drought and fuel moisture) and short-term (for example, wind conditions) cumulative timescales of fire drivers[27,28], as well as by human suppression, meaning that other conceptual models whereby low FRI results in higher-MRT PyC are plausible (models $H_2$ and $H_3$ in Fig. 1c,d).

To constrain the overall terrestrial fire carbon balance, several mechanisms that impose long-term carbon deficits on the terrestrial biosphere must be considered. First, the return of biomes to their pre-fire biomass state (Fig. 1a) requires a stable fire regime in which the biomass recovery interval (BRI; the time period of complete vegetation recovery) is shorter than the FRI. Violation of this condition (BRI < FRI) entails a natural or man-made change in the fire regime and an overall carbon deficit, representing a stepwise decrease in biomass carbon ($VC^-_{\Delta FiReg}$; Fig. 1a). Second, tropical rainforests exposed to drought[29] are vulnerable to episodes of vegetation-carbon (VC) mortality in the decades following fires (mortality can be up to 25% of VC[30,31]) and may not fully recover before the next fire event, so carbon is lost from the biome ($VC^-_{Mort}$). Third, in areas where the fire regime shifts to higher fire frequencies than the average for that vegetation type, large fractions of SOC can be lost through combustion, erosion and microbial mineralization ($SOC^-_{hfloss}$)[32]. Average topsoil SOC losses of >20% through this mechanism have been observed in grasslands and broadleaf forests globally[32]. Finally, PyC loss occurs through soil–atmosphere mineralization ($E^-_{PyC}$), and is the principal 'unknown' of this study. Equation (1) can then be expanded to include legacy fluxes from these changes in fire regimes to arrive at the net balance of post-fire carbon with respect to the terrestrial biosphere (Supplementary Section 1a,b):

$$E^-_{Fire} + E^-_{PyC} + SOC^-_{PyCExp} + VC^-_{\Delta FiReg} + VC^-_{Mort} + SOC^-_{hfloss} = U^+_{VCO_2} + SOC^+_{PyC} + PyC^+_{LW} \quad (2)$$

Mechanistic models of the terrestrial carbon cycle have thus far omitted these collective fire legacy carbon sinks and sources[33,34]. In this Article we integrate them into a global land surface model

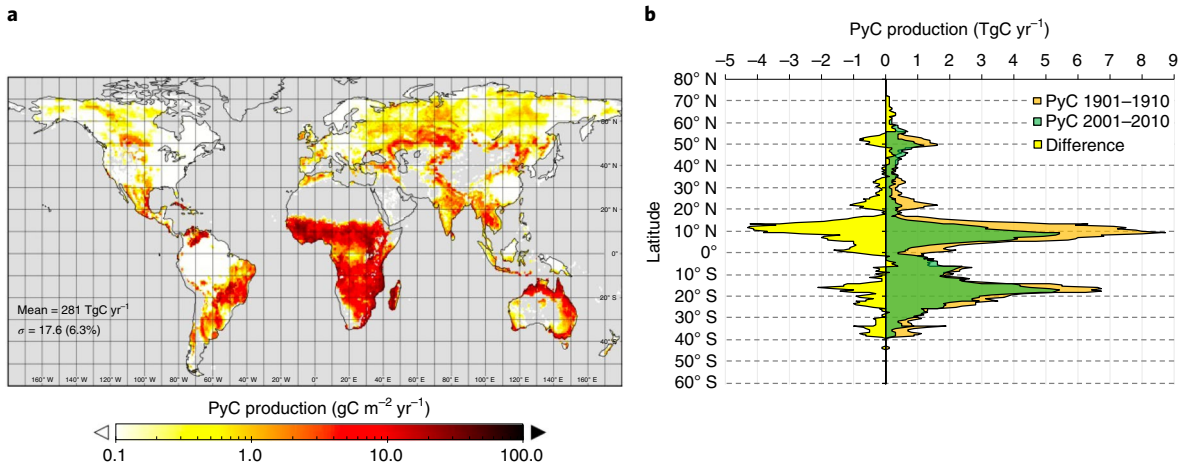


**Fig. 2 | Simulated PyC production and change over the period 1901–2010. a**, Map of global PyC production averaged over the entire simulation period (log gC $m^{-2}$ $yr^{-1}$), with global annual mean production and standard deviation indicated. **b**, Simulation averaged annual absolute PyC production summed per 0.5° latitude bin (TgC $yr^{-1}$) in 1901–1910 (orange) and 2001–2010 (green), with the difference (latter-former) shown in yellow.

(Methods and Supplementary Fig. 1) to provide an estimate of the annualized components of the fire legacy carbon cycle represented by equation (2). Specifically, we incorporate dynamic PyC production by fires into ORCHIDEE-MICT (Supplementary Figs. 1 and 2)[35–37] and run the model globally over 1901–2010 with prescribed vegetation and anthropogenic land-use changes (LUC), variable climate and historical $CO_2$ forcing (Methods and Supplementary Section 7). We investigate the spatio-temporal dynamics of the legacy fluxes over the twentieth century and quantify a fire carbon balance for global biomes (Methods). Carbon loss terms on the left side of equation (2) are derived offline from the model output (Methods). The FRI is determined for each grid cell and plant type (Supplementary Figs. 2–4 and Supplementary Table 1), as is vegetation-specific BRI (Supplementary Fig. 5 and Methods). We did not attempt to estimate the global mean PyC mineralization ($E^{-}_{PyC}$) due to a critical paucity of information on PyC residence times, their drivers and measurement across biomes[38–40]. Instead, we infer the maximum value of PyC mineralization that would lead to mass balance in equation (2). From this we infer a constraint on the global terrestrial PyC MRT ($MRT_{Terr.}$; Methods and Supplementary Text).

## Twentieth-century patterns of PyC production

Over the period 1901–2010 we estimate an average annual $SOC^{+}_{PyC}$ of 281 TgC-PyC $yr^{-1}$ (min.–max. range 188–424 TgC $yr^{-1}$; Methods), similar to a previous estimate for the period 1997–2016 driven by satellite observations of fire (256 (196–340) TgC $yr^{-1}$)[13]. The large interannual variations found (251–345 TgC $yr^{-1}$, $\sigma = 18$ TgC $yr^{-1}$) are symptomatic of trends over the twentieth century[41,42], when PyC production declined from an average of 298 to 269 TgC $yr^{-1}$ between the first and last three decades (Methods and Supplementary Text 7). The distribution of PyC production is consistent with that of fires generally, with the bulk occurring between 20° N and 30° S (Fig. 2a,b)[13]. However, twentieth-century declines in PyC production occurred mostly in the northern hemisphere, reflecting grassland LUC (Fig. 2b), and most localized PyC production gains were modelled in the southern tropics, resulting from increasing aridity and FRI (Supplementary Figs. 6–9).

Globally, fires affect biomes disproportionately, as ~80% of burning occurs in grassland-savannah-dominated regions[43], with 73–79% and 13–17% of modelled PyC production taking place in C4 and C3 (the photosynthetic pathways generally demarcating warm and cool climate grasses) grasslands, respectively, despite these accounting for ~30–40% of the global land surface[44,45]. This mismatch is caused by the evolutionary fire adaptations of grasslands, which preferentially allocate biomass to below-ground organs, allowing them to rapidly recover from disturbance[46,47] (BRI < 1–3 yr; refs. [27,48]). This enables the rapid return of fire events almost as soon as vegetation has recovered (FRI ≃ BRI) because tropical grassland-savannah fires are particularly fuel-limited[49], enabling them to thrive where tree cover is limited by environmental conditions[50]. This feature of grassland-savannah biomes is important to equation (2), because whereas loss terms $VC^{-}_{Mort}$ and $VC^{-}_{\Delta FiReg}$ are dependent on relative FRI:BRI, the production of refractory $SOC^{+}_{PyC}$ is an absolute quantity, meaning simply that the more fire there is, the more PyC is injected into the global soil mass (Fig. 1). The low FRI and BRI values mean that we find grassland-savannahs to be both the main PyC source (~250 TgC $yr^{-1}$) and, compared to other vegetation types, they pull the relative sink and source terms of equation (2) towards the former, in agreement with the relatively high PyC proportion of bulk SOC (5–30%) found in global grassland soils[51].

Our vegetation maps drive a −21% (−1.16 million (M) $km^2$) and −12% (−3.6 M$km^2$) net decline in C3 and (tropical) grassland-savannah area between the first and last decades of simulation (Supplementary Fig. 6). These changes lead to global decreases in PyC production (Fig. 2 and Supplementary Fig. 7) during the period 1901–2010, in spite of global forest PyC production doubling (Supplementary Fig. 10), as is consistent with a marked decrease in twentieth-century forest FRI (Supplementary Fig. 8). These PyC dynamics can be explained by bio-climatic and human factors that impact global patterns of burned area and fire emission (Supplementary Figs. 7 and 9). In grassland-savannah regions where fire emissions and PyC production decreased, reduced fuel loading through conversion to agriculture where burning is suppressed is likely a factor[2,41,52].

Conversion of native grassland to cultivation is visible in our simulated PyC production trends (Supplementary Fig. 7), consistent with global-scale[2,41,52] and localized observations in Argentina[53,54], northern Turkey[55,56], post-Soviet European and west Asian steppe[57], India[58,59], northeastern China[60,61], southeastern Australia[62,63], the Great Plains region[64] and central and northern Mexico[65]. PyC gain/loss is thus modulated by human management[66,67], largely responsible for an apparent decrease in fires in recent decades[41] and over the past century[42], as captured by modelled declines in global PyC production, mean fire radiation and duration (Supplementary Fig. 12). The net effect of these dynamics has been to approximately halve the partial fire carbon sink over the twentieth century (Supplementary Fig. 12).

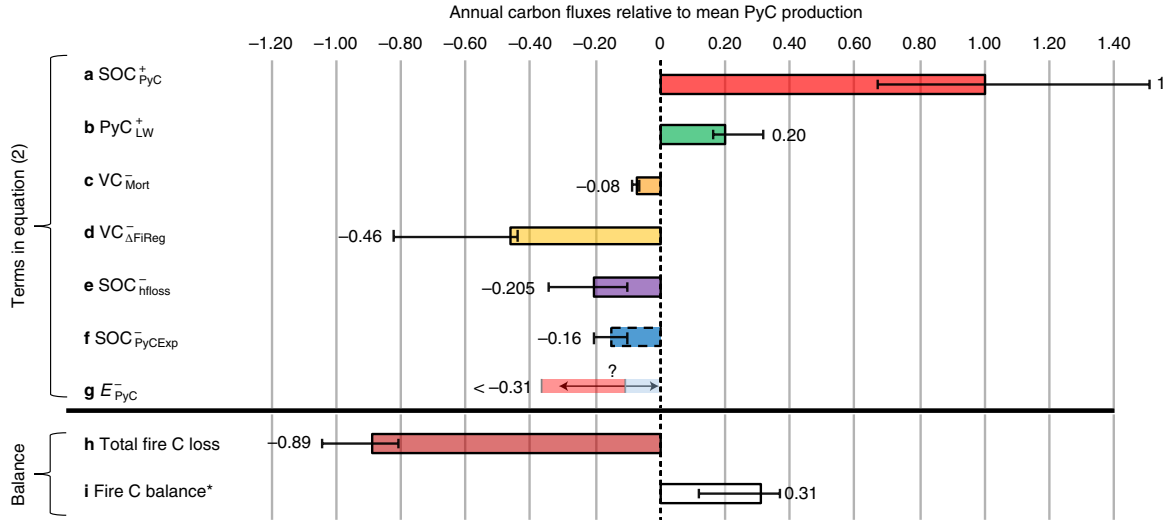


**Fig. 3 | Annual carbon fluxes of fire balance terms in equation (2). a**–**g**, Time-averaged estimates for the source and sink terms in equation (2), with the PyC mineralization loss quantity unknown (**g**), but constrained by the net fire carbon balance. The PyC aquatic export flux (**f**, $SOC^{-}_{PyCExp}$) is outlined by a dashed line to highlight that it is a terrestrial export flux, not an atmospheric flux. **h**,**i**, Aggregations of fire carbon losses relative to PyC production (sum of **c**–**f**) (**h**) and the fire carbon balance net of refractory PyC mineralization, that is, the sum of **a**,**b** and **c**–**f** (**i**). The asterisk in **i** emphasises that the fire C 'balance' is produced with no knowledge of PyC mineralization rates. Assuming steady state, maximum PyC mineralization (**g**) is thus equal to the residual (**i**), with the red and blue portions in **g** showing the range of maximum and minimum possible mineralization, respectively, and the arrows the possible mineralization range according to the reported central estimate. Error bars show the maximum and minimum time-averaged values for each balance component. These were calculated on the basis of the full range of values based out of the literature from which they were derived and subsequent calculations as detailed in the Methods. Details for error calculation of each component can be found in the Supplementary Information.

## Emerging constraints on fire's role in the carbon cycle

This study has simulated the legacy impacts of PyC production and fire carbon losses, a substantial advance on previous studies that considered these in isolation[13,32,68]. Over the period 1901–2010, average global legacy soil carbon sinks through refractory PyC production ($SOC^{+}_{PyC}$; 281 (188–424) TgC yr$^{-1}$) and lightweight PyC production ($PyC^{+}_{LW}$ = 56 (45–90) TgC yr$^{-1}$) are partially countered by legacy carbon sources from incomplete post-fire vegetation recovery ($VC^{-}_{\Delta FiReg}$ = 129 (123–231) TgC yr$^{-1}$; Supplementary Fig. 15 and Supplementary Table 4), high-frequency topsoil degradation ($SOC^{-}_{hfloss}$ = 57 (30–95) TgC yr$^{-1}$; Supplementary Fig. 16 and Supplementary Table 4), PyC aquatic export ($SOC^{-}_{PyCExp}$ = 44 (28–59) TgC yr$^{-1}$; Fig. 3, Supplementary Figs. 17 and 18 and Supplementary Table 4) and tropical drought-induced post-fire mortality ($VC^{-}_{Mort}$ = 21 (18–25) TgC yr$^{-1}$; Fig. 4, Supplementary Fig. 19 and Supplementary Table 4). Excluding $E^{-}_{PyC}$, the legacy fluxes are imbalanced and indicate a partial terrestrial carbon sink in PyC of 89 (34–104) TgC yr$^{-1}$ (Fig. 3 and Supplementary Table 4) assuming equation (2) is in a steady state. This implies a potential net fire 'carbon savings' rate of 0–4% of the ~2.2 PgC yr$^{-1}$ in fire $CO_2$ emissions. The magnitude of $E^{-}_{PyC}$ is solved as a residual of equation (2), meaning that if $E^{-}_{PyC}$ exceeds the net PyC accumulation of 89 (34–104) TgC yr$^{-1}$, then wildfires result in terrestrial PyC losses, and if $E^{-}_{PyC}$ is in balance with the net PyC accumulation (steady state), then we can constrain the global terrestrial mean residence time ($MRT_{Terr.}$) of PyC to a value of ~5,370 (1,966–14,100) years (Methods, Supplementary Section 1b and Supplementary Table 8), longer than in refs. [20,22,23], but smaller than in ref. [19].

Field and laboratory studies of PyC MRT have been sparse and restricted to a subset of biomes and fuel types, providing inconsistent central estimates with impractically large uncertainty ranges[19,20]. The temperature sensitivity of PyC decomposition is another key parameter for PyC turnover that is poorly understood, and whether PyC degradation is primarily mechanical or metabolic remains an open question[17], with implications for model representation and our understanding of the global soil biome[18,69]. Ultimately, the lack of a robust mechanistic description of PyC mineralization rates and drivers, perhaps attributable to inconsistencies in their measurement and definition, leads to PyC MRT estimates that vary by at least 40-fold (Supplementary Section 1b). Our steady-state constraint on PyC $MRT_{Terr.}$ (~5,370 yr) is in the range of values reported in a soil incubation experiment[19] and the radiocarbon age of riverine Py-POC[18]. Until addressed, this observational shortfall will frustrate efforts to reliably quantify or constrain the fire carbon balance (Supplementary Section 1).

## Regional distribution of legacy carbon fluxes

The global value of the residual carbon sink from changes in fire regimes and PyC masks substantial variability at the biome level.

**Fig. 4 | Global spatial distribution of the fire carbon balance. a**, Simulation average (1901–2010) annualized sources and sinks in the global fire carbon cycle, summed per 30° latitudinal band, in TgC yr$^{-1}$. Note that fire regime change and high-frequency fire SOC loss terms are disaggregated between forest (solid) and grass (hashed), and that the colour legend for each term is equivalent to that in Fig. 3. Values appended to bars denote the ratio of carbon gain:loss (>1 = carbon sink). **b**, Comparison of time-averaged grassland (right) and forest (left) fire carbon sources (red) and sinks (black) summed per 30° bin (as in **a**), in TgC yr$^{-1}$. Values appended to bars denote the ratio of C gain:loss (>1 = partial carbon sink, excluding $E^{-}_{PyC}$). **c**, Global map of the time-averaged, vegetation-summed residual in equation (2) (gC m$^{-2}$ yr$^{-1}$) for each pixel, where negative values indicate a carbon source and positive values a carbon sink. The balance is calculated as the net sum of equation (2), excluding the PyC mineralization term ($E^{-}_{PyC}$), which is constrained but unknown. Inset: a summary statistics table of the residual per plant type (mean, standard deviation and its percent mean value, concluding with the residual as a fraction of total $PyC_{SOC}$). EG, evergreen; RG, rain-green; SG, summer-green.

The largest absolute fire carbon gains and losses are simulated in the tropics (Fig. 4a). The net legacy carbon gain associated with PyC production is greatest in the tropics (+83 TgC yr$^{-1}$), although it is substantially offset by legacy carbon losses, most notably by incomplete vegetation recovery ($VC^{-}_{Mort}$), soil degradation ($SOC^{-}_{hfloss}$; Fig. 4c and Supplementary Figs. 8 and 16) and riverine export ($SOC^{-}_{PyCExp}$). The ratio of gains to losses is 1.2 in the Northern Hemisphere (NH) tropics and 1.7 in the Southern Hemisphere (SH) tropics, signifying

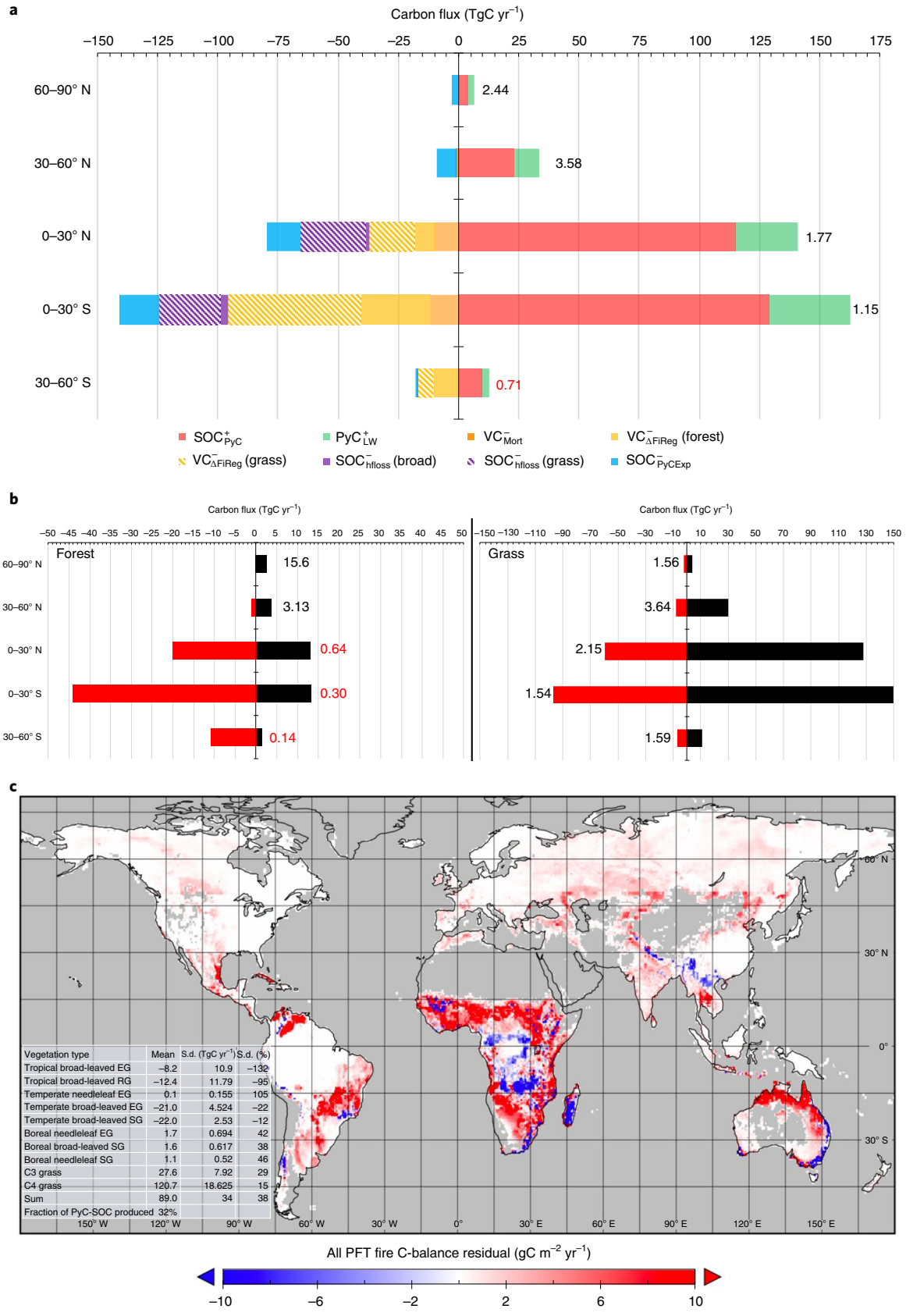

a potential for overall carbon sequestration depending on the magnitude of the PyC mineralization flux in these regions. Gains exceed losses in the tropics, predominantly due to tropical grassland-savannahs (gains:losses of 1.5 and 2.1 in the NH and SH, respectively), whereas losses substantially exceed gains in tropical forests (Fig. 4). Legacy carbon losses exceed legacy carbon gains in the southern extra-tropics even before the unconstrained losses of PyC are considered. Globally, the residual of the constrained fluxes is strongly on the sink side in grasslands ($+148\,TgC\,yr^{-1}$) but on the source side in forests ($-43\,TgC\,yr^{-1}$).

We show that most (73–79%) PyC production occurs in tropical grassland-savannah regions, through fires that also generate the highest mean global flame temperatures (~500 °C; Supplementary Table 2), implying that the majority of global PyC production may result in PyC with a high MRT, as conferred by the heat of charring (Fig. 1c,d and Supplementary Table 1)[14,70]. By contrast, tropical and temperate forest fires produce the highest maximal but lower average flame temperatures, consistent with the greater dependence of fire on fuel moisture than fuel availability in these regions (Fig. 1c). Overall, the model simulates the highest flame temperatures in semi-arid and higher-elevation regions in the 0–30° N/S range, implying one can expect a decreasing PyC-MRT gradient from tropics to poles.

Simulated fire temperatures (Supplementary Table 2) increase across biomes over the gradient from boreal (188 °C) to C3 grass (335 °C), tropical forest (353 °C), temperate forest (404 °C) and tropical grassland-savannah (501 °C), indicating that the relationship between flame temperature and fuel availability (Fig. 1c) is nonlinear and strongly modulated by climatic and fuel conditions[71], such that curves $H_1$–$H_3$ (Fig. 1c,d) cannot accurately represent the global relationship without additional dimensionality, such as plant trait impacts on flammability and flame intensity[72]. However, current understanding of PyC charring[14,70] allows us to propose that tropical grassland and savannah regions produce the greatest quantity of PyC of the greatest relative longevity, and that grassland and forest fires play contrasting functional roles in the terrestrial carbon balance.

## Towards a holistic view of fire's role in the carbon cycle

Legacy carbon sequestration fluxes driven by PyC production exceed legacy carbon losses through incomplete post-fire recovery, LUC and soil degradation. The overall impact of legacy carbon fluxes on the terrestrial carbon balance is nonetheless not constrained due to insufficient knowledge regarding PyC mineralization. We note that the riverine export of PyC to the global oceans ($SOC^{-}_{PyCExp}$) is also a conservative flux with respect to the atmospheric carbon balance; however, rates of PyC mineralization in oceanic pools are constrained at least as poorly as in the terrestrial domain[18,73]. The resolution of PyC mineralization fluxes in soils and sediments across the land-to-ocean continuum is thus a critical research frontier.

Our results highlight the regional complexity of legacy carbon fluxes from fires and challenges the narrative that fires are solely catastrophic phenomena[74], suggesting that their severity and the long-term extent of their destructiveness is highly dependent on both biome[75] and subtle shifts in fire regime characteristics. In forests, fire carbon losses can overwhelm PyC gains even without considering PyC mineralization. This is not surprising, particularly in the humid tropics, where tree species are ill-adapted to disturbance[76] and massive post-fire mortality is commonplace[29–31,76] (Supplementary Fig. 19). Globally, forest fire-induced carbon losses are compensated by the dynamics of grassland ignition, in the absence of which fire phenomena would impose a net terrestrial carbon source irrespective of PyC production. Without widespread grassland-savannah coverage in the tropics, the legacy effects of fires could not feasibly enhance terrestrial carbon storage—a result afforded by the capacity of grasses for fire recovery[77]. This emergent result coheres with studies suggesting that the co-evolution of grassland fire and herbivory, particularly in tropical grasslands, led to the formation of PyC-rich mollisols that may have been central to climatic cooling in geological time[47], and that evolution of vegetation types with fire may have been central to the trajectory of Earth's carbon and $O_2$ cycles[78].

The dependency of the fire carbon residual on vegetation composition has important implications for projected increases[9,79,80] in climate extremes[81–83], potentially increasing all terms in equation (2). The preservation/restoration of native grasslands may be an important vector for decreasing carbon losses from future fire activity in both temperate and tropical systems. Despite this, tropical grasslands have until recently been ignored in the landscape restoration and 'carbon farming' agenda[4,48,50,84,85].

This Article has attempted to further the understanding of fire's role in the Earth's carbon cycle by the identification and first-order quantification of multiple legacy terms of the fire carbon budget in a land surface model. We provide a benchmark for the maximum global PyC mineralization rate and show that, without widespread grassland-savannah coverage, fires would be a net global source of atmospheric carbon. We call for substantial investments in the understanding of PyC degradation and its drivers[18,69], in addition to improved estimates of legacy fire carbon fluxes. Reliable quantification of PyC mineralization and erosion, particularly over grasslands, remains the principal missing link in a holistic understanding of fire's role in the Earth system.

## Online content

Any methods, additional references, Nature Research reporting summaries, source data, extended data, supplementary information, acknowledgements, peer review information; details of author contributions and competing interests; and statements of data and code availability are available at https://doi.org/10.1038/s41561-021-00892-0.

Received: 13 December 2020; Accepted: 26 December 2021;
Published online: 10 February 2022

## References

1. Van Marle, M. J. E. et al. Historic global biomass burning emissions for CMIP6 (BB4CMIP) based on merging satellite observations with proxies and fire models (1750–2015). *Geosci. Model Dev.* **10**, 3329–3357 (2017).
2. Erb, K. H. et al. Unexpectedly large impact of forest management and grazing on global vegetation biomass. *Nature* **553**, 73–76 (2018).
3. Cook-Patton, S. C. et al. Mapping carbon accumulation potential from global natural forest regrowth. *Nature* **585**, 545–550 (2020).
4. Bastin, J. F. et al. The global tree restoration potential. *Science* **365**, 76–79 (2019).
5. Bowman, D. M. J. S. et al. Fire in the Earth system. *Science* **324**, 481–485 (2009).
6. Archibald, S. et al. Biological and geophysical feedbacks with fire in the Earth system. *Environ. Res. Lett.* **13**, 033003 (2018).
7. Mills, B. J. W., Belcher, C. M., Lenton, T. M. & Newton, R. J. A modeling case for high atmospheric oxygen concentrations during the Mesozoic and Cenozoic. *Geology* **44**, 1023–1026 (2016).
8. Lenton, T. M. in *Fire Phenomena and the Earth System: An Interdisciplinary Guide to Fire Science* (ed. Belcher, C. M.) 298–308 (Wiley, 2013).
9. Pechony, O. & Shindell, D. T. Driving forces of global wildfires over the past millennium and the forthcoming century. *Proc. Natl Acad. Sci. USA* **107**, 19167–19170 (2010).
10. Marlon, J. R. et al. Reconstructions of biomass burning from sediment-charcoal records to improve data-model comparisons. *Biogeosciences* **13**, 3225–3244 (2016).
11. Archibald, S., Staver, A. C. & Levin, S. A. Evolution of human-driven fire regimes in Africa.*Proc. Natl Acad. Sci. USA* **109**, 847–852 (2012).
12. Santín, C. et al. Towards a global assessment of pyrogenic carbon from vegetation fires. *Global Change Biol.* **22**, 76–91 (2016).
13. Jones, M. W., Santín, C., van der Werf, G. R. & Doerr, S. H. Global fire emissions buffered by the production of pyrogenic carbon. *Nat. Geosci.* **12**, 742–747 (2019).

14. Bird, M. I., Wynn, J. G., Saiz, G., Wurster, C. M. & McBeath, A. The pyrogenic carbon cycle. *Annu. Rev. Earth Planet. Sci.* **43**, 273–298 (2015).
15. Hammes, K. & Abiven, S. in *Fire Phenomena and the Earth System: An Interdisciplinary Guide to Fire Science* (ed. Belcher, C. M.) 157–176 (Wiley, 2013).
16. Schmidt, M. W. I. et al. Persistence of soil organic matter as an ecosystem property. *Nature* **478**, 49–56 (2011).
17. Lavallee, J. M. et al. Selective preservation of pyrogenic carbon across soil organic matter fractions and its influence on calculations of carbon mean residence times. *Geoderma* **354**, 113866 (2019).
18. Coppola, A. I. et al. Global-scale evidence for the refractory nature of riverine black carbon. *Nat. Geosci.* **11**, 584–588 (2018).
19. Kuzyakov, Y., Bogomolova, I. & Glaser, B. Biochar stability in soil: decomposition during eight years and transformation as assessed by compound-specific $^{14}C$ analysis. *Soil Biol. Biochem.* **70**, 229–236 (2014).
20. Singh, B. P., Cowie, A. L. & Smernik, R. J. Biochar carbon stability in a clayey soil as a function of feedstock and pyrolysis temperature. *Environ. Sci. Technol.* **46**, 11770–11778 (2012).
21. Masiello, C. A. & Druffel, E. R. M. Black carbon in deep-sea sediments. *Science* **280**, 1911–1913 (1998).
22. Santos, F., Torn, M. S. & Bird, J. A. Biological degradation of pyrogenic organic matter in temperate forest soils. *Soil Biol. Biochem.* https://doi.org/10.1016/j.soilbio.2012.04.005 (2012).
23. Zimmermann, M. et al. Rapid degradation of pyrogenic carbon. *Glob. Change Biol.* **18**, 3306–3316 (2012).
24. Jones, M. W. et al. Fires prime terrestrial organic carbon for riverine export to the global oceans. *Nat. Commun.* **11**, 2791 (2020).
25. Qi, Y. et al. Dissolved black carbon is not likely a significant refractory organic carbon pool in rivers and oceans. *Nat. Commun.* **11**, 5051 (2020).
26. Pausas, J. G. & Paula, S. Fuel shapes the fire-climate relationship: evidence from Mediterranean ecosystems. *Glob. Ecol. Biogeogr.* **21**, 1074–1082 (2012).
27. Archibald, S., Lehmann, C. E. R., Gómez-Dans, J. L. & Bradstock, R. A. Defining pyromes and global syndromes of fire regimes. *Proc. Natl Acad. Sci. USA* **110**, 6442–6447 (2013).
28. Abatzoglou, J. T., Williams, A. P., Boschetti, L., Zubkova, M. & Kolden, C. A. Global patterns of interannual climate-fire relationships. *Glob. Change Biol.* **24**, 5164–5175 (2018).
29. Brando, P. M. et al. Prolonged tropical forest degradation due to compounding disturbances: implications for $CO_2$ and $H_2O$ fluxes. *Glob. Change Biol.* **25**, 2855–2868 (2019).
30. Silva, C. V. J. et al. Drought-induced Amazonian wildfires instigate a decadal-scale disruption of forest carbon dynamics. *Phil. Trans. R. Soc. B* **373**, 20180043 (2018).
31. Withey, K. et al. Quantifying immediate carbon emissions from El Niño-mediated wildfires in humid tropical forests. *Phil. Trans. R. Soc. B* **373**, 20170312 (2018).
32. Pellegrini, A. F. A. et al. Fire frequency drives decadal changes in soil carbon and nitrogen and ecosystem productivity. *Nature* **553**, 194–198 (2018).
33. Reisser, M., Purves, R. S., Schmidt, M. W. I. & Abiven, S. Pyrogenic carbon in soils: a literature-based inventory and a global estimation of its content in soil organic carbon and stocks.*Front. Earth Sci.* **4**, 80 (2016).
34. Wei, X., Hayes, D. J., Fraver, S. & Chen, G. Global pyrogenic carbon production during recent decades has created the potential for a large, long-term sink of atmospheric $CO_2$. *J. Geophys. Res. Biogeosci.* **123**, 3682–3696 (2018).
35. Guimberteau, M. et al. ORCHIDEE-MICT (v8.4.1), a land surface model for the high latitudes: model description and validation. *Geosci. Model Dev.* **11**, 121–163 (2018).
36. Thonicke, K. et al. The influence of vegetation, fire spread and fire behaviour on biomass burning and trace gas emissions: results from a process-based model. *Biogeosciences* **7**, 1991–2011 (2010).
37. Yue, C. et al. Modelling the role of fires in the terrestrial carbon balance by incorporating SPITFIRE into the global vegetation model ORCHIDEE—Part 1: simulating historical global burned area and fire regimes. *Geosci. Model Dev.* **7**, 2747–2767 (2014).
38. Abiven, S. & Santín, C. Editorial: From fires to oceans: dynamics of fire-derived organic matter in terrestrial and aquatic ecosystems. *Front. Earth Sci* **7**, 31 (2019).
39. Santín, C., Doerr, S. H., Preston, C. M. & González-Rodríguez, G. Pyrogenic organic matter production from wildfires: a missing sink in the global carbon cycle. *Glob. Change Biol.* **21**, 1621–1633 (2015).
40. Santín, C. et al. Carbon sequestration potential and physicochemical properties differ between wildfire charcoals and slow-pyrolysis biochars. *Sci. Rep.* **7**, 11233 (2017).
41. Andela, N. et al. A human-driven decline in global burned area. *Science* **356**, 1356–1362 (2017).
42. Arora, V. K. & Melton, J. R. Reduction in global area burned and wildfire emissions since 1930s enhances carbon uptake by land. *Nat. Commun.* **9**, 1326 (2018).
43. Mouillot, F. & Field, C. B. Fire history and the global carbon budget: a 1°×1° fire history reconstruction for the 20th century. *Global Change Biol.* **11**, 398–420 (2005).
44. Gibson, D. *Grasses and Grassland Ecology. Annals of Botany* (Oxford Univ. Press, 2009).
45. Dixon, A. P., Faber-Langendoen, D., Josse, C., Morrison, J. & Loucks, C. J. Distribution mapping of world grassland types. *J. Biogeogr.* **41**, 2003–2019 (2014).
46. Bond, W. J. Ancient grasslands at risk. *Science* **351**, 120–122 (2016).
47. Retallack, G. J. Global cooling by grassland soils of the geological past and near future. *Annu. Rev. Earth Planet. Sci.* **41**, 69–86 (2013).
48. Leys, B. A., Marlon, J. R., Umbanhowar, C. & Vannière, B. Global fire history of grassland biomes. *Ecol. Evol.* **8**, 8831–8852 (2018).
49. Alvarado, S. T., Andela, N., Silva, T. S. F. & Archibald, S. Thresholds of fire response to moisture and fuel load differ between tropical savannas and grasslands across continents. *Glob. Ecol. Biogeogr.* **29**, 331–344 (2020).
50. Buisson, E. et al. Resilience and restoration of tropical and subtropical grasslands, savannas and grassy woodlands. *Biol. Rev.* **94**, 590–609 (2019).
51. Rodionov, A. et al. Black carbon in grassland ecosystems of the world. *Glob. Biogeochem. Cycles* **24**, GB3013 (2010).
52. Haberl, H., Erb, K. H. & Krausmann, F. Human appropriation of net primary production: patterns, trends and planetary boundaries. *Annu. Rev. Environ. Resources* **39**, 363–391 (2014).
53. Medan, D., Torretta, J. P., Hodara, K., de la Fuente, E. B. & Montaldo, N. H. Effects of agriculture expansion and intensification on the vertebrate and invertebrate diversity in the Pampas of Argentina. *Biodivers. Conserv.* **20**, 3077–3100 (2011).
54. González-Roglich, M., Swenson, J. J., Villarreal, D., Jobbágy, E. G. & Jackson, R. B. Woody plant-cover dynamics in Argentine savannas from the 1880s to 2000s: the interplay of encroachment and agriculture conversion at varying scales. *Ecosystems* **18**, 481–492 (2015).
55. Satir, O. & Erdogan, M. A. Monitoring the land use/cover changes and habitat quality using Landsat dataset and landscape metrics under the immigration effect in subalpine eastern Turkey. *Environ. Earth Sci.* **75**, 1118 (2016).
56. Şekercioğlu, Ç. H. et al. Turkey's globally important biodiversity in crisis. *Biol. Conserv.* **144**, 2752–2769 (2011).
57. Schierhorn, F. et al. Post-Soviet cropland abandonment and carbon sequestration in European Russia, Ukraine and Belarus. *Glob. Biogeochem. Cycles* **27**, 1175–1185 (2013).
58. Jaglan, M. S. & Qureshi, M. H. Irrigation development and its environmental consequences in arid regions of India. *Environ. Manage.* **20**, 323–336 (1996).
59. Joshi, A. A., Sankaran, M. & Ratnam, J. 'Foresting' the grassland: historical management legacies in forest-grassland mosaics in southern India, and lessons for the conservation of tropical grassy biomes. *Biol. Conserv.* **224**, 144–152 (2018).
60. Huang, F., Wang, P. & Zhang, J. Grasslands changes in the Northern Songnen Plain, China during 1954–2000. *Environ. Monit. Assess.* **184**, 2161–2175 (2012).
61. Zhou, Y., Hartemink, A. E., Shi, Z., Liang, Z. & Lu, Y. Land use and climate change effects on soil organic carbon in north and northeast China. *Sci. Total Environ.* **647**, 1230–1238 (2019).
62. Williams, N. S. G. Environmental, landscape and social predictors of native grassland loss in western Victoria, Australia. *Biol. Conserv.* **137**, 308–318 (2007).
63. Dowling, P. M. et al. Effect of continuous and time-control grazing on grassland components in south-eastern Australia. *Aust. J. Exp. Agric.* **45**, 369–382 (2005).
64. DeLuca, T. H. & Zabinski, C. A. Prairie ecosystems and the carbon problem. *Front. Ecol. Environ.* **9**, 407–413 (2011).
65. Ceballos, G. et al. Rapid decline of a grassland system and its ecological and conservation implications. *PLoS ONE* **5**, e8562 (2010).
66. Haugo, R. et al. A new approach to evaluate forest structure restoration needs across Oregon and Washington, USA. *For. Ecol. Manage.* https://doi.org/10.1016/j.foreco.2014.09.014 (2015).
67. DeLuca, T. H. & Aplet, G. H. Charcoal and carbon storage in forest soils of the Rocky Mountain West. *Front. Ecol. Environ.* **6**, 18–24 (2008).
68. Walker, X. J. et al. Increasing wildfires threaten historic carbon sink of boreal forest soils. *Nature* **572**, 520–523 (2019).
69. Bellè, S. L. et al. Key drivers of pyrogenic carbon redistribution during a simulated rainfall event. *Biogeosciences* **18**, 1105–1126 (2021).
70. Abney, R. B., Jin, L. & Berhe, A. A. Soil properties and combustion temperature: controls on the decomposition rate of pyrogenic organic matter. *Catena* **182**, 104127 (2019).
71. Bradstock, R. A., Hammill, K. A., Collins, L. & Price, O. Effects of weather, fuel and terrain on fire severity in topographically diverse landscapes of south-eastern Australia. *Landsc. Ecol.* **25**, 607–619 (2010).

72. Rogers, B. M., Soja, A. J., Goulden, M. L. & Randerson, J. T. Influence of tree species on continental differences in boreal fires and climate feedbacks. *Nat. Geosci.* **8**, 228–234 (2015).
73. Coppola, A. I. & Druffel, E. R. M. Cycling of black carbon in the ocean. *Geophys. Res. Lett.* **43**, 4477–4482 (2016).
74. Stenzel, J. E. et al. Fixing a snag in carbon emissions estimates from wildfires. *Glob. Change Biol.* **25**, 3985–3994 (2019).
75. Murphy, B. P., Prior, L. D., Cochrane, M. A., Williamson, G. J. & Bowman, D. M. J. S. Biomass consumption by surface fires across Earth's most fire prone continent. *Glob. Change Biol.* **25**, 254–268 (2019).
76. Brando, P. M. et al. Droughts, wildfires and forest carbon cycling: a pantropical synthesis. *Annu. Rev. Earth Planet. Sci.* **47**, 555–581 (2019).
77. Appezzato-da-Glória, B., Cury, G., Soares, M. K. M., Rocha, R. & Hayashi, A. H. Underground systems of *Asteraceae* species from the Brazilian Cerrado. *J. Torrey Bot. Soc.* **135**, 103–113 (2008).
78. Belcher, C. M. et al. The rise of angiosperms strengthened fire feedbacks and improved the regulation of atmospheric oxygen. *Nat. Commun.* **12**, 503 (2021).
79. Barbero, R., Abatzoglou, J. T., Larkin, N. K., Kolden, C. A. & Stocks, B. Climate change presents increased potential for very large fires in the contiguous United States. *Int. J. Wildl. Fire* **24**, 892–899 (2015).
80. Stephens, S. L. et al. Managing forests and fire in changing climates. *Science* **342**, 41–42 (2013).
81. Trenberth, K. E. Changes in precipitation with climate change. *Clim. Res.* **47**, 123–138 (2011).
82. Prein, A. F. et al. The future intensification of hourly precipitation extremes. *Nat. Clim. Change* **7**, 48–52 (2017).
83. Abatzoglou, J. T., Williams, A. P. & Barbero, R. Global emergence of anthropogenic climate change in fire weather indices. *Geophys. Res. Lett.* **46**, 326–336 (2019).
84. Silveira, F. A. O. et al. Myth-busting tropical grassy biome restoration. *Restor. Ecol.* **28**, 1067–1073 (2020).
85. Strassburg, B. B. N. et al. Global priority areas for ecosystem restoration. *Nature* **586**, 724–729 (2020).
86. Schmidt, H. P. et al. Pyrogenic carbon capture and storage. *GCB Bioenergy* **11**, 573–591 (2019).
87. Fu, Z. et al. Recovery time and state change of terrestrial carbon cycle after disturbance. *Environ. Res. Lett.* **12**, 104004 (2017).

## Methods

**Model description.** In this Article we apply PyC production to the IPSL Earth System Model, ORCHIDEE-MICT revision number 5308 (Supplementary Fig. 1), a widely used sub-branch of ORCHIDEE that is global in scope but includes some soil, hydrological and thermal processes specific to boreal regions[35,88,89], the use of which here will facilitate future assessments of PyC stocks in deep permafrost soils. At the core of the model is terrestrial biomass fixed by photosynthetic carbon uptake, performed by 13 plant functional types (PFTs) with distinct primary production, senescence and carbon dynamics[90]. Biomass is allocated to foliage, fruit, roots, above/below-ground sap, heart wood and carbon reserves, which are transferred to two reactivity-differentiated litter pools. ORCHIDEE-MICT is integrated with a model-specific version[37,91] of the SPITFIRE fire module[36,37,91], which takes the above-ground portion of these biomass components and allocates them to potential fire fuel classes differentiated by their potential time to combustion/oxidation. ORCHIDEE-SPITFIRE has been involved in multiple phases of FireMIP[92] and its predictions have been found to be within the range of those from available fire models[1,93–95]. Fire ignitions are controlled by lightning strikes and human ignitions, the latter of which are determined as a positive logistic function of population density. Vegetation flammability is determined by fuel and climatic conditions (the Nesterov index and fire danger index). Burned area is controlled by fire spread rate and fire duration, as influenced by vegetation flammability, and affects fire $CO_2$ emissions.

**Modelled PyC production.** PyC is produced in ORCHIDEE-MICT as a function of fuel class-specific fire $CO_2$ emissions using an adaptation of the apportioning between PyC production and fire $CO_2$ emissions estimate by Jones et al.[13], who posit a central literature-based prediction of ratios [$SOC_{PyC}$:$E_{CO2}$] of 0.261, 0.1 and 0.091 gPyC produced per gram of $CO_2$-C emitted for the three fuel classes of coarse woody fuels (CWFs), fine woody fuels (FWFs) and non woody fuels (NWFs), respectively. Uncertainty in PyC production (Fig. 3) is based on the bootstrapped 95% confidence interval range in ref. [13] for PyC production ratios ([$SOC_{PyC}$:$E_{CO2}$], gPyC-C per g $CO_2$-C) for CWF (0.176–0.389), FWF (0.064–0.153) and NWF (0.074–0.114) and applying the fractional difference of each bound from the central bound to PyC produced in the post-processing analysis. We apportion these to the four SPITFIRE fuel classes such that 1-h fuels → NWF, 10-h and 100-h fuels → FWF and 1,000-h fuels → CWF (Supplementary Fig. 1), where the hour term in SPITFIRE fuel classes refers to the order of magnitude of time required for the fuel to lose 63% of its moisture under idealized atmospheric conditions[36], determined effectively by the stem thickness of each biomass component of each PFT based on the 'average individual' of each woody PFT.

The carbon mass balance is maintained by removing PyC produced from other carbon pools. PyC produced is first subtracted from the fraction of biomass going to litter pools in that SPITFIRE timestep (one day). If PyC produced > biomass going to litter in that timestep, then the remaining quantity is taken from $CO_2$ emissions, the reduction of which recursively reduces the total PyC production. PyC is then introduced to the biosphere–pedosphere interface by its allocation to PyC-specific SOC reactivity pools, complementing the traditional CENTURY 3-pool model[96], with a 'slow PyC' pool composed of $PyC_{10h} + PyC_{100h}$ and a 'passive PyC' pool ($PyC_{1,000h}$), where the subscript refers to the source fuel class of PyC. In the present configuration, $PyC_{1h}$ does not enter into either of the SOC pools and, once produced, is instead added to the pool of dead biomass that becomes litter, which is then subject to normal model SOC dynamics (Supplementary Section 2).

Once produced, the PyC SOC pools are immediately redistributed equally amongst the top 2.1 cm of the model's vertically discretized soil layers to represent the initial translocation of PyC in the first year of production, following field observations from ref. [97]. PyC pools are not exchanged with one another or with the other SOC pools, and are subjected to vertical bio- and cryo-turbation processes in the soil and temperature- and moisture-dependent mineralization. Mineralization rates are equivalent to bulk MRTs of ~300 and ~3,000 yr for slow and passive PyC, respectively.

**Simulation configuration.** The simulations used for this study were forced with imposed historical 13-PFT vegetation (ESA-LUH2 v1.2), CRU-NCEP v8[98] climatology and atmospheric $CO_2$ concentrations at 0.5° resolution with SPITFIRE activated and hydrological river routing deactivated. Deforestation fires were deactivated and agricultural fires in the output ignored to simplify analysis. A 50-yr 'spinup' run on a loop of the years 1901–1920 for the above input forcing datasets was first performed to bring the biosphere and fire cycle to a quasi-steady state under the closest pre-twentieth-century climatology we can approximate with our climate data. The same model was then run continuously over the years 1901–2010. Fire carbon loss terms were estimated from derived variables in the simulation output. Deforestation fires were not activated in these simulations because the legacy effects of these events remain poorly understood and quantified.

**Estimating PFT-specific FRI.** PFT-specific FRI is defined as the interval between consecutive fires affecting a consistent area, which is not a standard output of ORCHIDEE and so was determined probabilistically. To do so, first we find the annual fractional fire contribution of each PFT ($f\mathrm{Fire}_{\mathrm{PFT}}$) to total $CO_2$ emissions:

$$f\mathrm{Fire}_{\mathrm{PFT}} = E\mathrm{Fire}_{\mathrm{PFT}}/\Sigma\,(E\mathrm{Fire}_{\mathrm{PFT}}) \quad (3)$$

From this, the probabilistic fire incidence per PFT, pixel and year can be estimated as

$$p(\mathrm{Fire})_{\mathrm{PFT}} = f\mathrm{PFT}_{\mathrm{Pix}} \times f\mathrm{Fire}_{\mathrm{PFT}} \times \mathrm{BA}_{\mathrm{Pix}} \quad (4)$$

where $p(\mathrm{Fire})_{\mathrm{PFT}}$ is the annual probabilistic fire incidence per PFT and pixel, and $f\mathrm{PFT}_{\mathrm{Pix}}$ the fraction of each PFT occupied by vegetation from a given PFT ($f\mathrm{PFT}_{\mathrm{Pix}}$), and $\mathrm{BA}_{\mathrm{Pix}}$ the burned area per pixel. Global probabilistic FRI (yr) for each pixel and PFT ($\mathrm{FRI}_{\mathrm{PFT}}$) over a given unspecifiable surface area (for example, one hectare) can then be calculated by dividing $p(\mathrm{Fire})_{\mathrm{PFT}}$ by the PFT-specific vegetated area, giving the probability that a given hectare occupied by a given PFT in that pixel is the one that burned that year. This is summed over the simulation years then divided over the simulation length (110 yr); 1 divided by this value gives the FRI:

$$\mathrm{FRI}_{\mathrm{PFT}} = 1/((\sum_{t=1}^{110}(p(\mathrm{Fire})_{\mathrm{PFT}}/(f\mathrm{PFT}_{\mathrm{Pix}} \times \mathrm{Area}_{\mathrm{Pix}})))/110) \quad (5)$$

The resulting gridded PFT-specific map is then adapted to set the maximum value of FRI at 1,000 yr across all PFTs, because this would largely result from insufficient sample size in time to adequately estimate the probabilistic FRI for these pixels/PFTs, resulting in strong potential skews in the FRI:BRI ratio, given that BRI itself rarely exceeds this value.

For estimating the average FRI value for each PFT, we employed a similar, yet PFT-specific approach. This was done for the same reasons as above, but with stricter thresholds for each PFT so as not to skew the average values with unrealistic probabilistic values. We used expert judgement based on both the literature and authors' expertise to set maximum realistic FRI values for each PFT of 2,000, 500, 200 and 100 years for tropical, temperate and boreal, C3 grass and C4 grasses, respectively, removing values above these for the mean estimate shown in the Supplementary Table. Further discussion of FRI estimation is provided in the Supplementary Text.

**Estimating PFT-specific BRI.** Biomass carbon recovery times (BRI, the time in which a given surface area recovers all of the biomass lost due to a disturbance event) are difficult to quantify and, to our knowledge, there is no global gridded product estimating disturbance and PFT-specific biomass recovery times. Here, we use a simple literature-based central value approach to approximate PFT-specific BRIs, modulated in space and time by the net primary production (NPP) of a pixel-specific PFT relative to the global median NPP of that PFT. We treated (1) C3 and C4 grasses, (2) all extra-tropical forest types and (3) tropical forests as separate categories. For (1) and (2), we assumed that, for a given pixel and year, carbon losses from fire can be recovered by the completion of that time interval, which itself varies by $\pm\beta$ as a function of the NPP experienced by that pixel relative to the global median NPP for that PFT:

$$\mathrm{BRI}_{\mathrm{Pix}}^{\mathrm{PFT}} = \mathrm{BRI}^{\mathrm{PFT}} \pm (\mathrm{BRI}^{\mathrm{PFT}} \times (\beta \times \mathrm{NPP}_{\mathrm{Pix}}^{\mathrm{PFT}}/\overline{\mathrm{NPPm}_{\mathrm{Global}}^{\mathrm{PFT}}})) \quad (6)$$

where $\mathrm{BRI}_{\mathrm{Pix}}^{\mathrm{PFT}}$ is the BRI per PFT, pixel and year, $\mathrm{BRI}^{\mathrm{PFT}}$ is the central, global value of BRI, $\beta$ is the fractional maximum variation of $\mathrm{BRI}_{\mathrm{Pix}}^{\mathrm{PFT}}$ from the central value, $\mathrm{NPP}_{\mathrm{Pix}}^{\mathrm{PFT}}$ is the annual NPP of that PFT in a specific pixel and $\overline{\mathrm{NPPm}_{\mathrm{Global}}^{\mathrm{PFT}}}$ is the time-averaged global median NPP of that PFT. For C3 and C4 grasses, we set $\mathrm{BRI}^{\mathrm{PFT}}$ at 2.5 and 1.5 yr, respectively, and $\beta$ at ±25%, based on literature-based estimates and the assumption that tropical grasses have high NPP and recovery rates. For forests we set the central $\mathrm{BRI}^{\mathrm{PFT}}$ for all non-tropical forest PFTs to the value reported in a literature review-based study (fig. 4d of ref. [87]) of 133 years, which we then allow to vary ($\beta$) by ±50% as a function of NPP relative to $\overline{\mathrm{NPPm}_{\mathrm{Global}}^{\mathrm{PFT}}}$ for each PFT. See Supplementary Information for a further discussion of the parameter choices.

**Estimating loss terms in equation (2).** *Loss of biospheric C due to fire regime change ($\overline{VC}_{\Delta FiReg}$).* This loss term is calculated for each PFT and includes net carbon losses from areas where the biospheric disturbance steady-state condition is not satisfied (BRI < FRI) as a result of a change in fire regime. We treat areas that experienced decreases in FRI of >10% between the first and last three decades of the simulation (Supplementary Fig. 7) as having exhibited a fire regime shift. We then estimate the system biomass loss per fire event for these areas as the BRI:FRI ratio in the year of the event multiplied by the total $CO_2$ emissions from a given PFT in that year's fires:

$$\mathrm{VC}_{\Delta\mathrm{FiReg}} = (\mathrm{BRI}_{\mathrm{PFT}}/\mathrm{FRI}_{\mathrm{PFT}}) \times E_{\mathrm{FCO_2}} \quad (7)$$

*Unrecovered drought-induced tropical post-fire mortality ($\overline{VC}_{Mort}^{-}$).* Here we extrapolate literature-derived estimates of tropical forest mortality losses derived from drought-induced fires to tropical forests globally and aggregate them annually. Existing literature estimates of this phenomenon are mostly drawn from the aftermath of El Niño events; however, given that drought is a continuous function of precipitation over time for a given biome and that (1) not all droughts are driven by El Niño and (2) not all tropical forests exist in zones in which

interannual climate is strongly characterized by El Niño activity, we extrapolate the findings of these field studies to all tropical forest regions characterized by severe or extreme drought according to a widely used drought index, tempering the index by taking only those regions where the index indicates these conditions on average over the course of a whole year. This gives a spatially explicit timeseries of post drought-fire tree mortality conditions. The unrecoverable vegetative carbon losses from that mortality are calculated on the basis of the relative timescales of fire return and vegetative recovery, as detailed in the following.

For this annual estimate we do not consider below-ground mortality losses, which are not estimated in the literature for this type of disturbance event. For the per-PFT total above-ground fraction of biomass allocation ($VC_{AG}^{PFT}$), we extract annual gridded biomass allocation terms and sum them over the total biomass allocated to all vegetation-carbon pools for each PFT ($fVC_{AG}^{PFT}$). The approximate total above- and below-ground vegetative biomass carbon of tropical PFTs for each grid cell and year are obtained by weighting the total vegetation carbon per pixel ($VC_{Total}^{PFT}$, a non-PFT-specific variable) by the fractional vegetation coverage of that pixel by that PFT ($fPFT_{Pix}$) and the relative NPP of that pixel ($NPP_{Pix}^{PFT}$) versus that of the pixel mean NPP ($\overline{NPP_{Pix}}$). Multiplying this by ($fVC_{AG}^{PFT}$) gives an estimate of the total above-ground annual biomass of the two tropical PFTs per pixel:

$$VC_{AG}^{PFT} = (VC_{Total}^{PFT} \times fPFT_{Pix} \times (NPP_{Pix}^{PFT}/\overline{NPP_{Pix}})) \times fVC_{AG}^{PFT} \quad (8)$$

Annual above-ground biomass maps are then filtered to mask out pixels where fire is absent in a given year. The resulting gridded $VC_{AG}^{PFT}$ dataset is then used to estimate the proportion of tropical vegetation affected by fire by multiplying the probability that a fire in a given pixel comes from a given PFT by the burned fraction of that PFT ($fBurn_{Pix}$):

$$FireVC_{AG}^{PFT} = VC_{AG}^{PFT} \times p(Fire)_{PFT} \times fBurn_{Pix} \quad (9)$$

To capture only those areas that may have experienced drought and hence drought-induced fire mortality, we employ the standardized precipitation index (SPI)[99], which derives a generic wet–dry index for any location by fixing a gamma probability density function to a timeseries of precipitation for a given location (in this case a given pixel containing a tropical forest PFT). To calculate the SPI for all grid cells over the timeseries of the study simulation, we use a pre-existing SPI function available in the NCAR command language (NCL)[100]. The SPI defines different thresholds for wet and dry conditions according to a continuous positive and negative scale, in which all SPI values under SPI < −1.5 are indicative of a location experiencing severe to extreme drought. Averaging the SPI annually, we mask out pixels in the dataset $FireVC_{AG}^{PFT}$ that do not satisfy the SPI < −1.5 condition. We then assume that total post-fire mortality loss is approximated from the mean literature value of −24.8% (±6.9%)[30] and define this fraction as the total carbon loss. However, because this biomass loss should be recoverable by the biosphere if BRI < FRI, only those pixels in which BRI > FRI are considered time-integrated losses, and only by the fraction given by the ratio of the two. To this loss is added the vegetative carbon-derived $CO_2$ emissions in the original drought-induced fire, which is similarly reduced by the (BRI:FRI) ratio. Thus, where SPI < −1.5 and BRI > FRI:

$$VC_{Mort}^{-} = \left(\left(FireVC_{AG}^{PFT} \times 0.248\right) + E_{FCO2}\right) \times (BRI_{PFT}/FRI_{PFT}) \quad (10)$$

For the $VC_{Mort}^{-}$ presented in the maps, figures and balance calculations, the total loss over the mortality period is calculated instantaneously for a given year, then spread into discrete annual loss terms over the cumulative period of dieback (Supplementary Text 6) Note that online tree mortality calculations made by ORCHIDEE-SPITFIRE due to crown and cambial scorching (Supplementary Fig. 1) are excluded from the calculation of this metric as their time frame (quasi-instantaneous) is inconsistent with the phenomena measured and reported in the literature on which the $VC_{Mort}^{-}$ term is based: drought-induced fire leading to persistent, widespread and non-saturating dieback over several decades owing to a variety of fire- and drought-related physiological weaknesses. Similarly, instantaneously killed biomass is a small fraction of the cumulative biomass loss instigated by drought-induced fires in tropical forests, according to the literature cited. Nevertheless, this quantity is in principle accounted for in the current iteration of $VC_{Mort}^{-}$.

*Soil carbon loss in areas with high-frequency fire* ($SOC_{hfloss}^{-}$). These losses are based on a recent empirical study[32] that found that large topsoil SOC losses are apparent across multiple sites globally in areas with high fire frequency, defined therein as anywhere with ~4.3 times the mean fire frequency for a given vegetation type, with losses of 27% and 21% accruing in areas of broadleaf and grassland vegetation. Here, and for each PFT defined as broadleaf forest and grassland, we approximate this loss spatially first by isolating those pixels that have an FRI that is ≥4.3 times that of the global average of that PFT (the threshold identified in ref. [32]). To account for the fact that the model simulation is transient and hence, in the early years of simulation, the topsoil carbon stocks will be unrealistically low, we only analyse $SOC_{hfloss}^{-}$ for the last 30 years of simulation (1981–2010). The loss over the top 19 cm of the soil column, based on the literature-derived soil loss parameters (27% ± 18% for broadleaf, 21% ± 12% for grassland)[32], is estimated for the relevant pixels during the period 1981–2010. Although SOC losses are not fully saturating in the Pellegrini et al. study of ref. [32], they are close enough that we assume that they represent total SOC losses due to high-frequency fires. Our estimate is limited because the loss term is predicated on the last 30 years of simulation, whereas FRI is based on the temporal range of the simulation (110 yr; see above). Thus, once annualized, the $SOC_{hfloss}^{-}$ estimate is constant over the whole simulation.

*PyC export losses within the inland water network* ($SOC_{PyCExp}^{-}$). A recent study has provided the first credible estimate to show that ~18 Tg of PyC in the dissolved phase (Py-DOC) flushes out of the global terrestrial landmass into the inland aquatic network annually[24], while estimates of similar particulate PyC (Py-POC) aquatic export are thought to total ~25 Tg C $yr^{-1}$ (ref. [18]). Here, we use ORCHIDEE-MICT to construct the first gridded, PFT-specific and spatio-temporally dynamic estimate of outflux. Jones et al.[24] estimated that boreal, tropical (<30° N/S) and temperate regions export 3.8 (±0.6), 12.4 (±4.9) and 1.8 (±0.8) Tg Py-DOC $yr^{-1}$, respectively, providing observational constraints on the total export of Py-DOC for latitude bins ($\sum DOC_{Bin}$).

To integrate $\sum DOC_{Bin}$ with the model output, we estimate the contribution of each PFT to global PyC-slow and PyC-passive soil carbon pool distributions and in doing so estimate the relative proportion of total DOC outflow originating from fires from each of these vegetation sources ($\sum DOC_{PFT}^{Pool}$). The relative global distribution of PyC produced is extracted from simulated global PyC soil pools in 1920, to approach historical distributions of PyC production. The fraction of total PyC per PFT and per PySOC pool ($f(PyC_{PFT}^{Pool})$) is calculated globally. The PFTs in $f(PyC_{PFT}^{Pool})$ are then split into boreal, temperate and tropical categories, and their fractional contribution to PyC of each bin to $PyC_{Slow}/PyC_{Passive}$ is calculated ($f(PyC_{PFT})_{Bin}^{Pool}$). C3 grasses incorporate temperate grasslands and tundra, so are split between by [temperate:boreal] surface area at 30–50° (~66%) and 50–90° N/S (~34%). The total mean absolute DOC flux (Tg C $yr^{-1}$) per pool and PFT ($\sum DOC_{PFT}^{Pool}$) is given by the following equation (Supplementary Table 1):

$$\sum DOC_{PFT}^{Pool} = f\left(PyC_{PFT}^{Pool}\right) \times f(PyC_{PFT})_{Bin}^{Pool} \times \sum DOC_{Bin} \quad (11)$$

We assume that Py-POC export occurs proportionally to Py-DOC export based on their literature-reported global export rates, such that total Py-POC + DOC export occurs at a rate 2.39 (=(18 + 25)/25) times that of Py-DOC. The total Py-SOC that is hydrologically mobilized from each soil pool ($Hyd.PyC_{PFT}^{Pool}$) is thus given by

$$\sum Hyd.PyC_{PFT}^{Pool} = \sum DOC_{PFT}^{Pool} \times 2.388 \quad (12)$$

The global export quantities are then distributed spatially over the globe in proportion to soil PyC stocks by a weighting based on the per-pixel fraction of the summed per-pool vertical PyC profile that is constituted by that pixel ($OUT_{PFT,Pixel}^{Pool}$):

$$OUT_{PFT,Pixel}^{Pool} = \sum DOC_{PFT}^{Pool} / \left(\frac{\sum_{3m}^{0m} PyC_{Pix}^{Pool}}{\sum_{3m}^{0m} PyC_{Globe}^{Pool}}\right) \quad (13)$$

This generates gridded estimates for mean annual PFT-specific DOC + POC export that are constrained by the global latitude-specific estimates reported in ref. [24]. Interannual variability is implemented by allowing export to vary for each pixel by up to 25% of the central value for each pixel in a manner that scales with deviation of annual precipitation from the median of the simulation period. Uncertainty is calculated by adjusting the DOC outflow values ($\sum DOC_{Bin}$) within the uncertainty ranges reported in ref. [24].

*Estimating modelled flame temperature and fire radiative power.* Approximate flame temperatures for each fire event are calculated online within the ORCHIDEE-SPITFIRE code. There, the reaction intensity (equation (9) in ref. [36]), the mean energy release rate per unit area of fire front (kJ $m^{-2}$ $min^{-1}$), which is a measure of flame power, is converted to temperature using the classical Boltzmann equation:

$$Q = \varepsilon \times k \times {T_F}^4 \quad (14)$$

where $Q$ is flame power, $\varepsilon$ is the emissivity of the combusting material (here assumed 0.9 for wood), $k$ is the Boltzmann constant and $T_F$ is the flame temperature (in K). The equation is solved for temperature and converted to celsius. Given that this is the first time, to our knowledge, that wildfire flame temperatures are directly estimated by an Earth system model, which are similarly not, to our knowledge, currently estimated by satellite products, we evaluate the flame temperature estimates simulated here by converting them to fire radiative power (FRP), a metric commonly employed by remote sensing practitioners for assessing fire intensity. For this purpose, we redeploy the equation proposed and employed by refs. [101,102], respectively, for returning FRP from MODIS satellite data to account for variations in pixel size:

$$FRP = A_s \times \beta \times \left({T_f}^8 - {T_b}^8\right) \quad (15)$$

where FRP (megawatt, MW) is fire radiative power, $A_s$ is the nominal pixel area evaluated at a scan or sample number, $\beta$ is a coefficient relevant to the MODIS spectral response, and $T_f$ and $T_b$ are the temperature of the fire pixel and a 'representative' or neighbouring background pixel without fire, respectively. For our purposes, we convert each pixel to km², retain the $\beta$ coefficient, and use the calculated flame temperature $T_F$ for $T_f$ and the input climatological data for $T_b$, respectively. These are discussed in the Supplementary Information.

*Back-of-the-envelope estimation of PyC bulk mean residence time.* The back-of-the-envelope estimates of minimum PyC MRT are made on the basis of a mix of existing stock and flow estimates, as well as the estimated maximum mineralization rate found in this study. This is calculated using the maximum PyC mineralization rate ($E^{-}_{PyC}$ (PgC yr$^{-1}$)), the estimated fraction of PyC in global SOC ($f$PyC$_{SOC}$), the estimated annual mineralization of bulk SOC ($E_{SOC}$ (PgC yr$^{-1}$)) and the estimated bulk mean MRT of SOC globally (MRT$_{SOC}$ (yr)). PyC MRT (MRT$_{PyC}$ (yr)) is estimated by

$$\mathrm{MRT}_{\mathrm{PyC}} = \left( f\mathrm{PyC}_{\mathrm{SOC}} / \left( \frac{E^{-}_{\mathrm{PyC}}}{E_{\mathrm{SOC}}} \right) \right) \times \mathrm{MRT}_{\mathrm{SOC}} \quad (16)$$

For the central estimate, we use the central value of the residual found here and central values for the above variables found in the literature such that $f$PyC$_{SOC}$ = 13.7% (ref. [33]), $E_{SOC}$ = 70 PgC yr$^{-1}$ (refs. [103,104]) and MRT$_{SOC}$ = 50 yr (ref. [16]). For the range reported in the main text we varied the calculation by the calculated range of the residual and by the range of $f$PyC$_{SOC}$ in global grassland soils reported in ref. [51] and summarized in Supplementary Table 8.

## Data availability

The data for figure reconstruction in addition to data for tropical post drought-fire mortality and pyrogenic production and aquatic export are available online as source data and Supplementary Information, respectively, and are also deposited in the Zenodo digital repository (https://www.zenodo.org; https://doi.org/10.5281/zenodo.5789942), which is managed by the European Organization For Nuclear Research (CERN) and OpenAIRE. Owing to file size limitations we are unable to deposit primary data (model output) online. These are archived on the Obelix cluster and the repository managed by LSCE/IPSL, which can be made available upon request by contacting the corresponding author. Source data are provided with this paper.

## Code availability

The source code for this version of ORCHIDEE-MICT is available via https://forge.ipsl.jussieu.fr/orchidee/wiki/GroupActivities/CodeAvalaibilityPublication/ORCHIDEE_Biochar (https://doi.org/10.14768/054193dc-a5b0-4a51-bd11-3812e8f12307; Bowring 2021). Please follow the online instructions for accessing the code. We suggest that interested parties contact the corresponding author for latest code versions containing bug fixes, improvements or cleaner code.
This software is governed by a CeCILL licence under French law and abiding by the rules of the distribution of free software. You can use, modify and/or redistribute the software under the terms of the CeCILL licence as circulated by CEA, CNRS and INRIA at the following URL: http://www.cecill.info (last accessed 20 November 2021).

## References


88. Zhu, D. et al. Improving the dynamics of Northern Hemisphere high-latitude vegetation in the ORCHIDEE ecosystem model. *Geosci. Model Dev.* **8**, 2263–2283 (2015).
89. Zhu, D. et al. Simulating soil organic carbon in Yedoma deposits during the Last Glacial Maximum in a land surface model. *Geophys. Res. Lett.* **43**, 5133–5142 (2016).
90. Krinner, G. et al. A dynamic global vegetation model for studies of the coupled atmosphere-biosphere system. *Glob. Biogeochem. Cycles* **19**, GB1015 (2005).
91. Yue, C., Ciais, P., Cadule, P., Thonicke, K. & Van Leeuwen, T. T. Modelling the role of fires in the terrestrial carbon balance by incorporating SPITFIRE into the global vegetation model ORCHIDEE—Part 2: carbon emissions and the role of fires in the global carbon balance. *Geosci. Model Dev.* **8**, 1321–1338 (2015).
92. Hantson, S. et al. The status and challenge of global fire modelling. *Biogeosciences* **13**, 3359–3375 (2016).
93. Hantson, S. et al. Quantitative assessment of fire and vegetation properties in simulations with fire-enabled vegetation models from the Fire Model Intercomparison Project. *Geosci. Model Dev.* **13**, 3299–3318 (2020).
94. Li, F. et al. Historical (1700–2012) global multi-model estimates of the fire emissions from the Fire Modeling Intercomparison Project (FireMIP). *Atmos. Chem. Phys.* **19**, 12545–12567 (2019).
95. Forkel, M. et al. Emergent relationships with respect to burned area in global satellite observations and fire-enabled vegetation models. *Biogeosciences* **16**, 57–76 (2019).
96. Parton, W. J., Stewart, J. W. B. & Cole, C. V. Dynamics of C, N, P and S in grassland soils: a model. *Biogeochemistry* **5**, 109–131 (1988).
97. Singh, N. et al. Transformation and stabilization of pyrogenic organic matter in a temperate forest field experiment. *Glob. Change Biol.* **20**, 1629–1642 (2014).
98. Viovy, N. *CRUNCEP Version 7—Atmospheric Forcing Data for the Community Land Model* (Research Data Archive at the National Center for Atmospheric Research, Computational and Information Systems Laboratory, 2018); https://doi.org/10.5065/PZ8F-F017
99. Mckee, T. B. T. et al. The relationship of drought frequency and duration to time scales. In *Proc. Eighth Conference on Applied Climatology* 179–184 (American Meteorological Society, 1993).
100. *The NCAR Command Language, Version 6.6.2* (UCAR/NCAR/CISL/TDD, 2019).
101. Freeborn, P. H., Wooster, M. J., Roy, D. P. & Cochrane, M. A. Quantification of MODIS fire radiative power (FRP) measurement uncertainty for use in satellite-based active fire characterization and biomass burning estimation. *Geophys. Res. Lett.* **41**, 1988–1994 (2014).
102. Giglio, L. *MODIS Collection 5 Active Fire Product User's Guide Version 2.5* (Science Systems and Applications, 2013).
103. Huang, N. et al. Spatial and temporal variations in global soil respiration and their relationships with climate and land cover. *Sci. Adv.* **6**, eabb8508 (2020).
104. Warner, D. L., Bond-Lamberty, B., Jian, J., Stell, E. & Vargas, R. Spatial predictions and associated uncertainty of annual soil respiration at the global scale. *Glob. Biogeochem. Cycles* **33**, 1733–1745 (2019).


## Acknowledgements

S.P.K.B. was supported by Swiss National Science Foundation (SNSF) grant no. SNSF 649 200021–178768 and would like to thank C. Yue, J. Chang and R. Lauerwald for discussions relating to ORCHIDEE modifications. M.W.J. was supported by the European Commission Horizon 2020 project VERIFY (grant no. 776810). P.C. was co-funded by the European Space Agency Climate Change Initiative ESA-CCI RECCAP2 project 1190 (ESRIN/ 4000123002/18/I-NB).

## Author contributions

S.P.K.B. and S.A. designed the study. S.P.K.B. performed the code implementation in ORCHIDEE, set up the simulations and processed the output used for this study. M.W.J. provided access to data and insight into the PyC production factors used in the simulations. P.C. and B.G. provided additional input to the coding, study design and data processing. All authors contributed to the interpretation of the results. S.P.K.B. wrote the manuscript and produced the figures, M.W.J. made substantial additions to the text. All authors contributed to final modifications of the manuscript.

## Competing interests

The authors declare no competing interests.

## Additional information

**Supplementary information** The online version contains supplementary material available at https://doi.org/10.1038/s41561-021-00892-0.

**Correspondence and requests for materials** should be addressed to Simon P. K. Bowring.

**Peer review information** *Nature Geoscience* thanks David Bowman, Kirsten Thonicke and the other, anonymous, reviewer(s) for their contribution to the peer review of this work. Primary Handling Editor: Xujia Jiang and Rebecca Neely, in collaboration with the *Nature Geoscience* team.